Geophysical and Astrophysical Fluid Dynamics
Vol. xx, No. xx, 2018, 1–24

The onset of thermo-compositional convection in rotating spherical shells

LUIS SILVA[1], JAMES F. MATHER and RADOSTIN D. SIMITEV[2]

School of Mathematics and Statistics, University of Glasgow – Glasgow G12 8QQ, UK

(*July 9, 2018*)

Double-diffusive convection, driven by both thermal and compositional buoyancy, in a rotating spherical shell can behave in a rather large number of distinct ways, often distinct from that of the single diffusive system. In order to understand how the differences in thermal and compositional molecular diffusivities determine the dynamics of thermo-compositional convection we investigate numerically the linear onset of convective instability in a double-diffusive setup. We construct an alternative equivalent formulation of the non-dimensional equations where the linearised double-diffusive problem is described by an effective Rayleigh number, Ra, measuring the amplitude of the combined buoyancy driving, and a second parameter, α, measuring the mixing of the thermal and compositional contributions. This formulation is useful in that it allows for the analysis of several limiting cases and reveals dynamical similarities in the parameters space which are not obvious otherwise. We analyse the structure of the critical curves in this $\mathrm{Ra} - \alpha$ space, explaining asymptotic behaviours in α, transitions between inertial and diffusive regimes, and transitions between large scale (fast drift) and small scale (slow drift) convection. We perform this analysis for a variety of diffusivities, rotation rates and shell aspect ratios showing where and when new modes of convection take place.

Keywords: double-diffusive convection, buoyancy-driven instabilities, planetary cores

1. Introduction

Convection in a rotating spherical fluid shell provides one of the fundamental models we have for understanding the large-scale motions and the magnetic fields of many geophysical, planetary and astrophysical systems, see (Glatzmaier 2013, Jones 2011, Busse and Simitev 2015). In Earth's outer core, for instance, convection is driven by both thermal and compositional buoyancy. Earth's core is composed mostly of iron and nickel, alloyed to lighter elements, supposedly sulphur, oxygen and hydrogen (Jeanloz 1990). Heat is continually lost to outer space causing secular cooling and establishing a thermal gradient that can drive thermal convection in the outer core. In addition, secular cooling causes freezing of iron onto the inner core, a process in which both latent heat and light material are released giving rise to additional thermal and chemical buoyancy (Jacobs 1953, Braginsky 1963). Both buoyancy components are important when modelling the geodynamo. Indeed, recent estimates of thermal conductivity for iron at core conditions (Pozzo et al. 2012, Davies et al. 2015) confirm that outer core convection cannot be driven by thermal buoyancy alone. It is estimated that the compositional contribution to the buoyancy flux in the Earth's core is around 80% (Lister and Buffett 1995). To model thermo-compositional convection Braginsky and Roberts (1995) and simultaneously Lister and Buffett (1995) suggested that temperature and concentration can be combined into an single “co-density” field. The co-density formulation has since been widely used in numerical simulations of the geodynamo and planetary dynamos, see reviews (Jones 2011, Christensen and Wicht 2015). However, the co-density formulation requires that a single

[1] lacsilva@gmail.com
[2] Radostin.Simitev@glasgow.ac.uk

set of effective boundary conditions, a single effective distribution of sources and a single effective value of the diffusility of the co-density variable must be used. While various modelling assumptions to that effect can be made, e.g. see attempts of Hori et al. (2012) to propose models for geophysically realistic thermo-compositional boundary conditions, of Olson et al. (2017), Takehiro and Sasaki (2018) to model stratification, and of Christensen (2015) to model a snow zone on Ganymede, it is not clear how well these can capture the distinct properties of separate heat and composition which diffuse at significantly different rates. Only handful of studies have employed a 'double-diffusive' formulation where both temperature and composition are included as separate fields. Breuer et al. (2010) and Trümper et al. (2012) found that the convective flows change significantly depending on the dominant driving component and reported that dynamo structures are also affected. In a double-diffusive model of Mercury's dynamo Manglik et al. (2010) observed that when thermal and compositional buoyancy are of equal intensity, finger convection penetrates the upper layer enhancing the poloidal magnetic field as compared to co-density cases. Exploring a geodynamo model Takahashi (2014) also concluded that the morphology of the obtained poloidal field is determined by the balance of thermal and compositional driving.

A systematic study of the linear onset of rotation double-diffusive convection is needed as a prerequisite for a detailed understanding of the behaviour of turbulent dynamos driven by thermal and compositional buoyancy. Indeed it is often found that the properties of convection at onset provide much insight to finite-amplitude convection (Simitev and Busse 2003, Busse and Simitev 2006). While the study of purely thermal convection has a long and distinguished history, without prejudice we only refer to the recent monograph of Zhang and Liao (2017) and the extensive list of references therein, the thermo-compositional case has received little attention in this context. By taking into account that heat diffuses much faster than chemical elements Busse (2002) used the small gap rotating cylindrical annulus model to show that the interaction of two components can significantly facilitate convection. Investigating the linear onset of double-diffusive convection in a rotating cylindrical annulus with conical caps Simitev (2011) found that the neutral surface describing the onset of convection in this case has an essentially different topology from that of the well-studied purely thermal case. In particular, due to an additional "double-diffusive" eigenmode, neutral curves are typically multi-valued and form regions of instability in the parameter space which may be entirely disconnected from each other. It was also observed that while known asymptotic expressions for the critical Rayleigh number and frequency derived by Busse (2002) describe the onset of convection over an extended range of non-asymptotic parameter values but do not capture the full complexity of the critical curves. Net et al. (2012) studied numerically the influence of an externally enforced compositional gradient on the onset of convection of a mixture of two components in a rotating fluid spherical shell. These authors considered both positive and negative compositional gradients and found that the influence of the mixture is significant in both cases. The aim of the present article is to extend and complement the latter studies and to contribute to a detailed linear analysis of the double-diffusive convection problem in the geometry of a rotation spherical shell. Indeed, this is needed as both the parameter space and the space of valid modelling assumptions that can be made is very large. Our model is mathematically similar to these of Busse (2002) and Simitev (2011) but is set in a spherical geometry. In contrast to Net et al. (2012), we consider the stress-free case for the velocity boundary conditions and internal rather than differential heating. Similarly to Net et al. (2012) we allow for both a stabilizing compositional gradient which may occur for instance, in lower main-sequence stars with heated helium-rich core surrounded by lighter hydrogen layers (Kippenhahn et al. 2012), as well as destabilising compositional gradients relevant, for instance, in the in the case of the Earth's core where solidification with release of light component takes place.

The article is organised as follows. We start by reviewing the mathematical set-up used to estimate the parameters of the system at onset in section 2. In section 3 we introduce a formalism that allows us to measure the combined effect of the thermal and compositional buoyancy and to better understand the convective processes that occur. Section 4 proceeds to describe the competition of eigenmodes that leads to the formation of the global critical curves for onset. The remaining sections 5, 6 and 7 are devoted to describing the onset of convection depending on the Prandtl and Coriolis numbers and aspect ratio, respectively. A summary of the results and conclusions is presented in section 8.

2. Mathematical formulation and numerical solution

We investigate the onset of thermo-compositional convection in a rotating spherical shell. The shell has thickness $d = r_o - r_i$, where r_o and r_i are the inner and the outer radii, respectively and rotates about an axis aligned with the z direction at a constant rate Ω. The unit vectors pointing in the z-direction and in the radial direction are denoted by $\mathbf{k}$ and $\mathbf{r}$, respectively and $r\mathbf{r}$ is then the position vector. The material within the spherical shell is assumed to be an incompressible fluid solution, with constant kinematic viscosity ν, thermal diffusivity κ, and chemical diffusivity D. The density ρ of the fluid is assumed to depend linearly on changes in composition and temperature with first order expansion coefficients α_C and α_T, respectively. We employ the Boussinesq approximation where the variation in density is assumed important only when they affect the gravitational force $-\rho\gamma r\mathbf{r}$, with γ a constant. In order to study the effects induced by the very different values of the thermal and of the chemical diffusivity in isolation from other effects, we follow (Busse 2002, Net et al. 2012) and disregard any differences in boundary conditions and in source-sink distribution for the temperature and concentration. Static profiles $T(r)$ and $C(r)$ of temperature and concentration with radial gradients $\partial_r T = -\beta_T r$ and $\partial_r C = -\beta_C r$, where β_T and β_C are constant densities of uniformly distributed sources, exists when temperatures and concentrations are fixed at the boundaries.

Using d^2/ν as the unit of time, d as the unit of length, $T^* = \beta_T d^2\nu/\kappa$ as the unit of temperature and $C^* = \beta_C d^2\nu/D$ as the of concentration arrive at the following linearised equations in adimensional units,

$$\partial_t \mathbf{u} = -\tau\mathbf{k}\times\mathbf{u} - \nabla\pi + (\mathrm{R_t}\Theta + \mathrm{R_c}\chi)r\mathbf{r} + \nabla^2\mathbf{u}, \tag{1a}$$

$$\partial_t\Theta = \mathrm{Pr}^{-1}\nabla^2\Theta - \mathbf{u}\cdot\nabla T, \tag{1b}$$

$$\partial_t\chi = \mathrm{Sc}^{-1}\nabla^2\chi - \mathbf{u}\cdot\nabla C, \tag{1c}$$

where $\mathbf{u}$ is the flow velocity, π is the generalized pressure, Θ is the temperature anomaly and χ is the compositional anomaly from the static reference states T and C, respectively. The non-dimentional parameters that appear in the equations are defined in Table 1. Note that, here, the scale for the composition, C^*, is inversely proportional to D. This is in contrast with the work of Simitev (2011) who scales C^* with κ. As a consequence, the compositional Rayleigh numbers present in this paper must be scaled by a factor of the *Lewis* number, $\mathrm{Le} = \kappa/D$, when compared to the latter work. Temperature and composition anomalies are set to vanish at the spherical boundaries and stress-fee boundary conditions are imposed for velocity. Except when otherwise mentioned, the equations are solved for a spherical shell with an inner to outer radius ratio of $\eta = 0.35$.

Since the velocity vector is solenoidal, we take advantage of the poloidal-toroidal decomposition

$$\mathbf{u} = \mathbf{u}_P + \mathbf{u}_T = \nabla\times\nabla\times\mathcal{S}(r\mathbf{r},t)\mathbf{r} + \nabla\times\mathcal{T}(r\mathbf{r},t)\mathbf{r}, \tag{2}$$

so that the poloidal and toroidal components $\mathbf{u}_P$ and $\mathbf{u}_T$ of the velocity $\mathbf{u}$ can be represented by a toroidal scalar function $\mathcal{T}(r\mathbf{r},t)$ and a poloidal scalar function $\mathcal{S}(r\mathbf{r},t)$ similarly to the

Parameter	**Definition**
Coriolis Number	$\tau = \Omega d^2/\nu$
Thermal Rayleigh Number	$\mathrm{R_t} = \alpha_T \gamma d^4 T^*/\nu^2$
Compositional Rayleigh Number	$\mathrm{R_c} = \alpha_C \gamma d^4 C^*/\nu^2$
Thermal Prandtl Number	$\mathrm{Pr} = \nu/\kappa$
Compositional Prandtl Number (Schmidt Number)	$\mathrm{Sc} = \nu/D$
Radius Ratio	$\eta = r_i/r_o$

Table 1. Adimensional model parameters. For brevity in the text we often speak of "Prandtl numbers" when we refer to both the Prandtl and the Schmidt numbers.

temperature and the compositional anomaly $\Theta(r\mathbf{r}, t)$ and $\chi(r\mathbf{r}, t)$. Each scalar quantity is then assumed to obey the linear Fourier mode ansatz in time

$$\mathcal{X}(r\mathbf{r}, t) = \tilde{\mathcal{X}}(r\mathbf{r}, \omega)\ \exp(it(\omega - i\Gamma)),$$

where ω is the frequency of oscillation (or drift rate) and Γ is the growth rate. The system will be stable so that any perturbation will decay if Γ is less than zero. Otherwise, a perturbation will grow exponentially over time, in which case the system is convectively unstable. Operating on Equation (1a) by $\mathbf{r}\cdot\nabla\times$ and by $\mathbf{r}\cdot\nabla\times\nabla\times$ four scalar equations describing the system are obtained

$$(i\omega + \Gamma)(\nabla^2 - 2r\partial_r)(\nabla_H^2 \tilde{\mathcal{S}}) \tag{3a}$$
$$= -\tau\mathbf{r}\cdot\nabla\times\nabla\times(\mathbf{k}\times\tilde{\mathbf{u}}) + \nabla_H^2(\mathrm{R_t}\tilde{\Theta} + \mathrm{R_c}\tilde{\chi}) + \mathbf{r}\cdot\nabla\times(\nabla\times(\nabla^2\tilde{\mathbf{u}})),$$

$$(i\omega + \Gamma)(\nabla_H^2 \tilde{\mathcal{T}}) = -\tau\mathbf{r}\cdot\nabla\times(\mathbf{k}\times\tilde{\mathbf{u}}) + \mathbf{r}\cdot\nabla\times(\nabla^2\tilde{\mathbf{u}}), \tag{3b}$$

$$(i\omega + \Gamma)\tilde{\Theta} = \mathrm{Pr}^{-1}\nabla^2\tilde{\Theta} - \tilde{\mathbf{u}}\cdot\nabla T, \tag{3c}$$

$$(i\omega + \Gamma)\tilde{\chi} = \mathrm{Sc}^{-1}\nabla^2\tilde{\chi} - \tilde{\mathbf{u}}\cdot\nabla C, \tag{3d}$$

where the horizontal Laplacian is defined as

$$\nabla_H^2 f = \nabla^2 f - \frac{1}{r^2}\frac{\partial}{\partial r}\left(r^2\frac{\partial f}{\partial r}\right),$$

and where for brevity in the text we have left some terms with $\tilde{\mathbf{u}}$ unexpanded.

To find the marginal convective stability where $\Gamma = 0$, each scalar quantity is further expanded in terms of spherical harmonics for the angular part. Due to the linearity of the equations and of the orthogonality properties of spherical harmonics individual azimuthal wave numbers m decouple and can be investigated one at a time. To complete the spatial discretisation of the problem in the radial direction we follow (Zhang and Busse 1987, Ardes et al. 1997) and expand all scalar unknowns $\tilde{\mathcal{X}}(r\mathbf{r})$ are trigonometric functions obeying the boundary conditions. After computing the appropriate Galerkin projection integrals numerically Equations (3) take the matrix form

$$(i\omega + \Gamma)\,[A]_{n,l}\begin{bmatrix}\tilde{s}_{n,l,m}\\ \tilde{t}_{n,l,m}\\ \tilde{\theta}_{n,l,m}\\ \tilde{\chi}_{n,l,m}\end{bmatrix} = [B]_{n,l}\begin{bmatrix}\tilde{s}_{n,l,m}\\ \tilde{t}_{n,l,m}\\ \tilde{\theta}_{n,l,m}\\ \tilde{\chi}_{n,l,m}\end{bmatrix}, \tag{4}$$

for fixed m, with sums being carried out over the degree of the associated Legendre polynomials

l and the index of the radial functions n. Matrices A and B are of the form

$$[A]_{n,l} = \begin{bmatrix} \square & \varnothing & \varnothing & \varnothing \\ \varnothing & \square & \varnothing & \varnothing \\ \varnothing & \varnothing & \square & \varnothing \\ \varnothing & \varnothing & \varnothing & \square \end{bmatrix}, \quad [B]_{n,l} = \begin{bmatrix} \square & \square & \square & \square \\ \square & \square & \varnothing & \varnothing \\ \square & \varnothing & \square & \varnothing \\ \square & \varnothing & \varnothing & \square \end{bmatrix}, \tag{5}$$

where squares represent non-null blocks. A triangular truncation of the sums is chosen such that the same number of radial functions and associated Legendre polynomials is used (Zhang and Busse 1987, Ardes et al. 1997),

$$2n + l - m + 2 \leq 3 + 2N, \tag{6}$$

with N an integer bigger than 2. N represents the required resolution for the calculation and always set to values higher than 10 and as close as feasibly possible to m. Equation (4) can then be solved for the complex eigenvalues $(i\omega + \Gamma)$ using standard numerical eigenvalue methods implemented in the NAG library[1].

Once the eigenvalue problem (4) is solved for a set of fixed parameter values non-trivial numerical extremization and continuation problems must be tackled in order to follow the critical threshold curve in the parameter space. The numerical code for the solution of the problem can be obtained via (Silva and Simitev 2018).

3. An effective Rayleigh-number formalism

Multivalued critical curves for the onset of thermo-compositional convection in related problems were reported by Simitev (2011) and Net et al. (2012). Our analysis confirms that this is the case in the present setting as illustrated by Figure 1 below. In this section, we propose a new adimensional parameter, Ra, that, similarly to the pure thermal case, can be used to measure criticality with respect to the onset of convection while at the same time to avoid the difficulties associated with finding the extrema of multivalued critical curves. The associated transformation of the governing linearised equations has the further advantage in addressing two important limiting cases.

The momentum equation (1a) can be transformed by representing the buoyancy force in the form

$$(\mathrm{R_t}\ \Theta + \mathrm{R_c}\ \chi)\, r\mathbf{r} = \mathrm{Ra}\, (\cos\alpha\ \Theta + \sin\alpha\ \chi)\, r\mathbf{r}, \tag{7}$$

with α varying between $-\pi$ and π and Ra being an effective positive Rayleigh number related to the thermal and the compositional Rayleigh numbers by

$$\mathrm{Ra} = \sqrt{\mathrm{R_t}^2 + \mathrm{R_c}^2}. \tag{8}$$

We refer to α the *Rayleigh angle* as it corresponds to an angle in the $\mathrm{R_t}$-$\mathrm{R_c}$plane. It is computed from the thermal and the compositional Rayleigh numbers using

$$\alpha = \mathrm{atan2}(\mathrm{R_c}/\mathrm{R_t}),$$

where the function $\mathrm{atan2}(x, y)$ is defined for $x \in \mathbb{R}$, $y \in \mathbb{R}$ as the principal argument $\mathrm{Arg}(z)$ of the complex number $z = x+iy$, a notation used in many programming languages. The value of $\alpha = 0$ corresponds to pure thermal convection and $\alpha = \pi/2$ to pure compositional convection. The typical co-density approach corresponds to $\alpha = \pi/4$ with $\mathrm{Pr} = \mathrm{Sc}$. We also remark that this parametrisation has several advantages over previous solutions such as the once proposed by Breuer et al. (2010) and Trümper et al. (2012) These authors considered a total Rayleigh

[1]The NAG Library, The Numerical Algorithms Group (NAG), Oxford, United Kingdom `www.nag.com`.

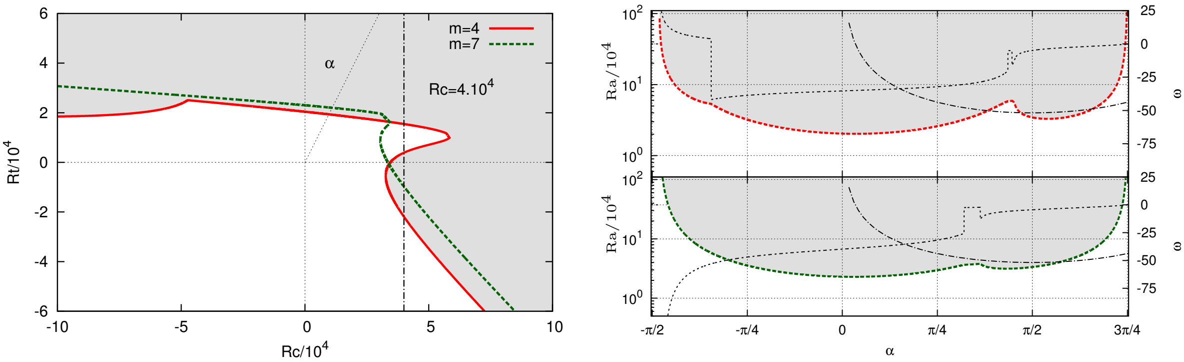

Figure 1. (left) The null curves for $m = 4$ and $m = 7$ at $\tau = 1.2 \times 10^3$, $\mathrm{Pr} = 1$ and $\mathrm{Sc} = 10$ in the $\mathrm{R_t} - \mathrm{R_c}$ plane. Null growth rate points in Figure 2 correspond to the null points on a cut at $\mathrm{R_c} = 4 \times 10^4$ marked as a thin dot-dashed vertical line. (middle) The null curve and oscillation frequency for $m = 4$. (right) The null curve and oscillation frequency for $m = 7$. Thin dot-dashed curves represent curves of $\mathrm{R_c} = 4 \times 10^4$. In all panels thin dashed lines are the frequency of oscillation ω. Shaded areas are regions where convection can exist.

number constructed as the simple sum of the thermal and compositional Rayleigh numbers. That is a very good approximation for the cases when the Prandtl and the Schmidt numbers are equal $\mathrm{Pr} = \mathrm{Sc}$ but fails when they are even only marginally different. In more practical terms, this new generalised Rayleigh number is strictly positive, which allows for plots in logarithmic scale. Adding to that, analysis of the critical curve at very high driving regimes can now be transferred to the analysis of the asymptotes in α. Finally, the interpretation of systems with negative Compositional Rayleigh numbers e.g., (Squyres et al. 1983, Röttger et al. 1994) can also now be shifted to the analysis of the regions in $\mathrm{Ra} - \alpha$ space where strong driving is required.

We now define a new set of dynamical variables Ψ and Ψ' and static reference profiles Ξ and Ξ' using the transformations

$$\Psi = \Theta \cos\alpha + \chi \sin\alpha, \qquad \Psi' = \Theta \cos\alpha - \chi \sin\alpha, \tag{9a}$$

$$\Xi = T \cos\alpha + C \sin\alpha, \qquad \Xi' = T \cos\alpha - C \sin\alpha, \tag{9b}$$

with the inverses being

$$\Theta \cos\alpha = \frac{\Psi + \Psi'}{2}, \qquad \chi \sin\alpha = \frac{\Psi - \Psi'}{2}. \tag{10}$$

By substituting these expressions into Equations (1a)-(1c) and adding and subtracting Equations (1b) and (1c), we arrive at the transformed problem

$$\partial_t \mathbf{u} = -\tau \mathbf{k} \times \mathbf{u} - \nabla \pi + \mathrm{Ra} \Psi r \mathbf{r} + \nabla^2 \mathbf{u}, \tag{11a}$$

$$\partial_t \Psi = \mathrm{P_+}^{-1} \nabla^2 \Psi + \mathrm{P_-}^{-1} \nabla^2 \Psi' - \mathbf{u} \cdot \nabla \Xi, \tag{11b}$$

$$\partial_t \Psi' = \mathrm{P_+}^{-1} \nabla^2 \Psi' + \mathrm{P_-}^{-1} \nabla^2 \Psi - \mathbf{u} \cdot \nabla \Xi', \tag{11c}$$

with effective Prandtl numbers defined as

$$\mathrm{P_+}^{-1} = \frac{\mathrm{Pr}^{-1} + \mathrm{Sc}^{-1}}{2}, \qquad \mathrm{P_-}^{-1} = \frac{\mathrm{Pr}^{-1} - \mathrm{Sc}^{-1}}{2}. \tag{12}$$

Note that, whereas the number $\mathrm{P_+}^{-1}$ is strictly positive, the number $\mathrm{P_-}^{-1}$ can now be negative thus providing a means of concentrating rather than diffusing the fields Ψ or Ψ'. This mechanism, as we shall see, can drive convection at lower than expected Rayleigh numbers and at very large scales.

Formulation (11) allows us to consider two important limiting cases. First, we note that the transformed momentum Equation (11a) only depends on the field Ψ. A consequence of this decoupling is that, in the case of $\mathrm{P_-}^{-1}$ approaching 0, the system will behave as if driven only by one buoyancy generating field. This situation arises when Pr is close or equal to Sc and thus, we obtain the traditional co-density approximation. We will analyse this case in more depth in sections 5.1 and 5.2.

A second limiting case studied further in the paper is found found when the Prandtl numbers are significantly different in magnitude. In this case

$$\mathrm{P_+}^{-1} \approx \frac{1}{2}\max(\mathrm{Pr}^{-1}, \mathrm{Sc}^{-1}) \approx \mathrm{Pr}^{-1}/2, \tag{13a}$$

$$\mathrm{P_-}^{-1} \approx \pm\frac{1}{2}\max(\mathrm{Pr}^{-1}, \mathrm{Sc}^{-1}) \approx \pm\mathrm{Pr}^{-1}/2, \tag{13b}$$

with $\mathrm{Pr}^{-1} = \max(\mathrm{Pr}^{-1}, \mathrm{Sc}^{-1})$ and $\mathrm{P_-}^{-1}$ being negative when $\mathrm{Pr}^{-1} < \mathrm{Sc}^{-1}$. Then Equations (11).b,c can be rewritten approximately as

$$\partial_t \Psi \approx \frac{\mathrm{Pr}^{-1}}{2}\nabla^2(\Psi \pm \Psi') - \mathbf{u}\cdot\nabla\Xi, \tag{14a}$$

$$\partial_t \Psi' \approx \frac{\mathrm{Pr}^{-1}}{2}\nabla^2(\Psi' \pm \Psi) - \mathbf{u}\cdot\nabla\Xi'. \tag{14b}$$

With all other parameters fixed, the changes to the critical value of Ra can only be due to different behaviours of the system with respect to α. This case will be analysed more in depth in section 5.3 where we will also explore the effects of Pr on the curves $\mathrm{Ra}_c(\alpha)$.

4. Construction of global critical curves

The introduction of the equation of concentration in system (1) leads to an increased number of eigenmodes in comparison to the pure thermal case as noted by Simitev (2011) and as most directly apparent by the increased dimension of the of the eigenvalue problem (4). The new eigenmodes correspond to modes of convection not present in the case of pure thermal convection. Figure 2 shows a comparison between the eigenmodes of the double-buoyant, double-diffusive case and the eigenmodes of the purely thermal case for two particular azimuthal wave numbers $m = 4$ and $m = 7$ with $\mathrm{R_c} = 4 \times 10^5$, $\tau = 1.2 \times 10^3$ and $\mathrm{Sc} = 10$. Two types of eigenmodes are observed in the former case – (a) ones that are present in the purely thermal case but are now modified, and (b) additional ones that have no counterpart in the purely thermal case. Next, for each azimuthal wave number m, convection will arise when the upper envelope of the curves of the growth rates is above zero for any eigenmode, illustrated by shaded regions in Figure 2. The addition of compositional effects clearly modifies the eigenmodes, notably in the way of promoting convection at lower thermal Rayleigh numbers. Moreover, as in the case of the cylindrical annulus studied by Simitev (2011), the additional compositional eigenmodes will, in certain circumstances, form new regions of convective instability that may be disconnected from the main convective region as shown in the left panel of Figure 2. In this case, the semblance of an disconnected island of instability forms for the particular azimuthal mode. Whether the region will remain disconnected depends on the overlap with the instability regions of the eigenmodes of the rest wave numbers. This leads us to a discussion of the construction of global critical curves below.

A composite critical curve is thus obtained for each azimuthal wave-number as shown in Figure 3. There, we can also see that the critical curves for different values of m intersect and overlap allowing convection for only certain m-values and not for others. Convective instability occurs at the lowest value of Ra for among the critical curves for the separate values of m.

The physical system corresponding to Equations (1) will start convecting with a most unstable azimuthal wave-number that depends on the angle α, conveniently measured clockwise from the $\mathrm{R_t}$-axis. Some azimuthal wave-numbers will contribute to large portions of the global

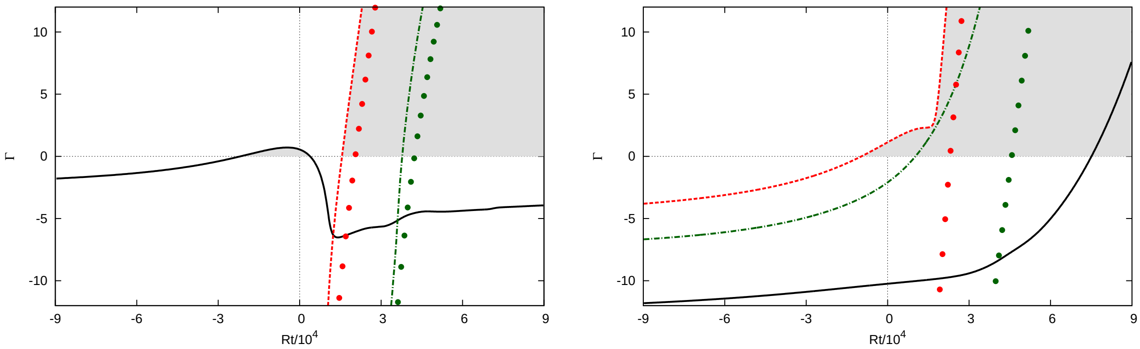

Figure 2. Eigenmodes with a positive growth rate in some part of the parameter space for the azimuthal wave numbers $m = 4$ (left panel) and $m = 7$ (right panel) at $\mathrm{R_c} = 4 \times 10^3$, $\tau = 1.2 \times 10^3$ and $\mathrm{Sc} = 10$. Dots represent the pure thermal eigenmodes and dot-dashed lines the corresponding compositionally modified modes. The solid black curves show additional modes are due composition that has no corresponding purely thermal counterpart. Shaded areas are regions of convective instability.

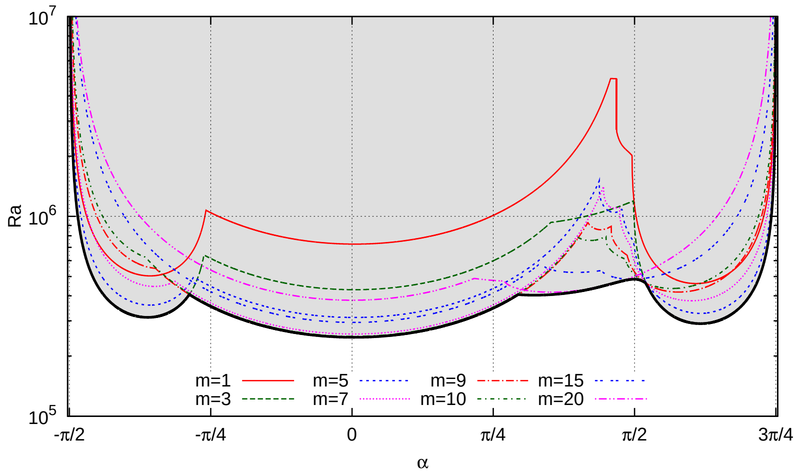

Figure 3. Constructing the global critical curve by choosing the lower envelope of the curves for all m's. Results are for $\eta = 0.35$, $\tau = 10^4$, $\mathrm{Pr} = 1.0$ and $\mathrm{Le} = 100$. Only curves for selected m's are shown. The global curve is shown as the thick black line.

critical curve ($m = 9$ in Figure 3); others will contribute only point-wisely (e.g. $m = 15$) and others not at all (e.g. $m = 1$).

To aid the discussion on the dependence of parameters in the following sections we recall known asymptotic expressions for the critical Rayleigh and azimuthal wave numbers and drift-rate for a rapidly rotating spherical shell with $\tau^{1/2} \gg 1$. In terms of our dimensionless parameters these relations are

$$\begin{aligned} R_{\mathrm{crit}} &= 7.252 \left(\frac{2P\tau}{1+P}\right)^{4/3} (1-\eta)^{10/3}, \quad m_{\mathrm{crit}} = 0.328 \left(\frac{2P\tau}{(1+P)}\right)^{1/3} (1-\eta)^{-2/3}, \\ \omega_{\mathrm{crit}} &= -0.762 \left(\frac{4\tau^2}{P(1+P)^2}\right)^{1/3} (1-\eta)^{2/3}. \end{aligned} \tag{15}$$

Here, P can just refer to either the thermal Prandtl number Pr or the Schmidt number Sc. For the cases of $P \to \infty$ (i.e. either $\mathrm{Pr} \to \infty$ or $\mathrm{Sc} \to \infty$) we obtain

$$\begin{aligned} &\lim_{P\to\infty} R_{\mathrm{crit}} = 7.252(2\tau)^{4/3}(1-\eta)^{10/3}, \quad \lim_{P\to\infty} m_{\mathrm{crit}} = 0.328(2\tau)^{1/3}(1-\eta)^{-2/3} \\ &\lim_{P\to\infty} \omega_{\mathrm{crit}} \to 0. \end{aligned} \tag{16}$$

The derivatives with respect to P of Equation (15) are all positive

$$\frac{dR_{\rm crit}}{dP} > 0, \quad \frac{dm_{\rm crit}}{dP} > 0, \quad \frac{d\omega_{\rm crit}}{dP} > 0, \tag{17}$$

with all derivatives tending to zero as $P \to \infty$. We therefore expect that in the region $0 \leq \alpha \leq \pi/2$ where $\mathrm{R_t}$ and $\mathrm{R_c}$ are positive and specifically at $\alpha = 0$ (purely thermal case) and $\alpha = \pi/2$ (purely compositional case) that as we increase Pr from 10^{-1} that we should see an increase in Ra and m towards limiting values and a decrease in the magnitude of ω towards zero. Equation (15) also shows that $R_{\rm crit} \propto \tau^{4/3}$, $m_{\rm crit} \propto \tau^{1/3}$ and $\omega_{\rm crit} \propto \tau^{2/3}$. therefore it is expected that as τ is increased, the critical Rayleigh and wave numbers and drift-rate should also increase. Finally, it is evident from Equation (15) that $R_{\rm crit} \propto (1-\eta)^{10/3}$, $m_{\rm crit} \propto (1-\eta)^{-2/3}$ and $\omega_{\rm crit} \propto (1-\eta)^{2/3}$. Therefore, by increasing η, it is expected that the critical Rayleigh number and drift-rate should decrease but that the critical azimuthal wave number should increase. Equations (15) are only valid for $P\tau \gg 1$ and have limited accuracy for low Prandtl numbers.

5. Dependence on the Prandtl number

5.1. *The case of equal Prandtl numbers*

The simplest case to analyse is the case of equal Prandtl and Schmidt number as it reverts to the results of the onset of pure thermal convection. When temperature and composition have the same diffusivities, the thermal and compositional Prandtl numbers will be the same. Then, despite convection being affected differently by the different quantities, composition and temperature will evolve in a similar manner. Recalling Equations (11), the number of adimensional parameters can be reduced by assuming equal Prandtl and Schmidt numbers i.e. $\mathrm{Pr} = \mathrm{Sc}$. Equation (11a) depends only on Ψ and Equation (11b) is now decoupled from Equation (11c) with Ψ' being then little more than a passive tracer for the flow. The system reduces to the well known co-density approach. The critical Rayleigh curve then reduces to a straight line of the form $\mathrm{R_t} = -\mathrm{R_c} + \mathrm{Ra_0}$ in the $\mathrm{R_t} - \mathrm{R_c}$ plane, as proposed by Breuer et al. (2010), and to

$$\mathrm{Ra}_c = \frac{\mathrm{Ra_0}}{\cos\alpha + \sin\alpha} \tag{18}$$

in the $\mathrm{Ra} - \alpha$ plane. All curves are symmetric with respect to $\alpha = \pi/4$ (equal Rayleigh numbers) and grow to infinity with asymptotes at $\alpha = -\pi/4$ and $\alpha = 3\pi/4$ as illustrated in Figure 4.

The factor $\mathrm{Ra_0}$ depends, in general, on the values of τ, Pr and η; in this section we are only concerned with the effects of varying Pr. Equations (11a) and (11b) show that the larger Pr becomes, the smaller its influence is. The coefficient $\mathrm{Ra_0}$ should then become independent of Pr at large values of this parameter. We will call this regime the advective regime. At Prandtl numbers much smaller than one the process of diffusion takes over and prevents small scale convection from growing. Then, much larger scales dominate and then the onset of convection occurs at lower values of the Rayleigh numbers. This is the diffusive regime. The transition between these two regimes occurs at $\mathrm{Pr} = 0.1$ as (Zhang and Busse 1987, Zhang 1994, Plaut and Busse 2005). Figure 4a illustrates this situation by showing the null curves of Ra as a function of α for Pr varying between $\mathrm{Pr} = 10^{-5}$ (lower curves) to $\mathrm{Pr} = 10^{4}$ (higher curves). As the most unstable azimuthal wave-number m and drift-rate ω are constant along the curves we show the variation of these with respect to varying Prandtl number Pr as well as the critical Rayleigh number for the co-density case $\mathrm{Ra_0}$. Computations were carried at $\tau = 10^4$. The curves in Figure 4b cluster in the limits $\mathrm{Pr} \to 0$ and $\mathrm{Pr} \to \infty$, with small m's ($m = 2$)

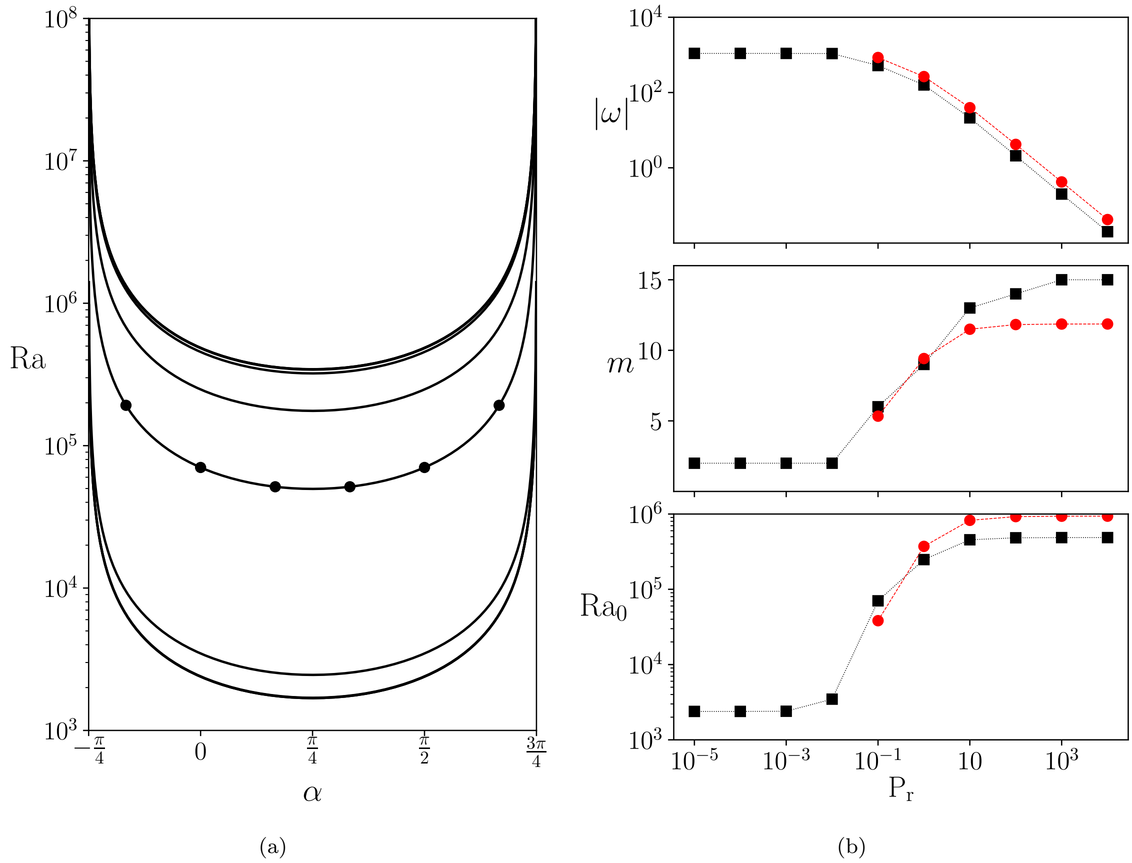

Figure 4. (a) Critical curves of Ra as a function of α for Pr varying from $\mathrm{Pr} = 10^{-5}$ (lowest curve) to $\mathrm{Pr} = 10^4$ (highest curve) in increasing multiples of ten. The circle markers indicate the curve plotted for $\mathrm{Pr} = 0.1$ where the transition from inertial to viscous convection occurs (b) Variation of the critical Rayleigh number, Ra_0, (bottom panel), most unstable wave-number, m, and magnitude of the drift-rate, $|\omega|$, with respect to Pr. Computations were carried out for $\tau = 10^4$.

for $\mathrm{Pr} \to 0$ and large wavenumbers m's ($m \geq 14$) for $\mathrm{Pr} \to \infty$. The behaviour in the limit of $\mathrm{Pr} \to \infty$ agrees well with the asymptotic estimate of Equation (15) which shows that the asymptotic limiting values are approached for the critical Rayleigh and wave numbers and drift rates in that limit and as seen in Figure 4b (circle markers). Asymptotic relations exist for low Prandtl numbers are given in (Busse and Simitev 2004) it will be of interest to verify whether the critical values of the Rayleigh and wave numbers as well as drift-rate plotted in Figure 4b approach these limit values also.

For low values of the Pr, convection takes the form of equatorially-attached cells centred in the shell and exhibits a strong clockwise drift, with the strongest radial flow at the equator mid-shell and undeformed large scale convection cells attached to the outer boundary. A very abrupt transition to rotating convection happens at $\mathrm{Pr} = 0.1$. Above this value, convection columns appear with much smaller azimuthal scale. They have a structure like the double-humped mode described by Ardes et al. (1997). The changes in behaviour continue until the traditional curved convection cells are recovered from a Prandtl number just above 0.2 and upwards. At this stage, the onset of convection happens throughout the whole exterior of the tangent cylinder except for a very thin layer near the outer boundary. For values of Pr larger than unity the onset of convection takes place in the middle of the shell.

5.2. *Small departures from the* $\mathrm{Pr} = \mathrm{Sc}$ *regime.*

We now depart from the co-density case of a "single-diffusive" fluid that is characterised by equal Prandtl numbers. In this section we start by developing a first order approximation to Equations (11) that will allow for the analysis of small departures from the regime of $\mathrm{Pr} = \mathrm{Sc}$. Figures 5a and b show the effects of setting the values of Sc just below and just above $\mathrm{Pr} = 1.0$, respectively. Again, calculations were performed at $\tau = 10^4$. Firstly, however, consider a small number, δ, such that $|\delta| \ll 1$ and the assumption that the thermal and compositional Prandtl numbers are close in value such that, $\mathrm{Sc} = \mathrm{Pr}(1 + \delta)$. We can then approximate the transformed Prandtl numbers of Equations (12) to first order by

$$\mathrm{P_+}^{-1} \approx \frac{\mathrm{Pr}^{-1}}{2}\,(2-\delta)\,, \qquad \mathrm{P_-}^{-1} \approx \frac{\mathrm{Pr}^{-1}}{2}\delta. \tag{19}$$

As expected, $\mathrm{P_+}^{-1}$ is always much larger than $\mathrm{P_-}^{-1}$ but the latter is still finite. If this approximation is substituted into Equations (11b) we find that to terms of $O(\delta)$ the approximate equations are

$$\partial_t \Psi = \mathrm{Pr}^{-1}\nabla^2\Psi - \mathbf{u}\cdot\nabla\Xi + \frac{\delta}{2}\mathrm{Pr}^{-1}\nabla^2(\Psi' - \Psi), \tag{20a}$$

$$\partial_t \Psi' = \mathrm{Pr}^{-1}\nabla^2\Psi' - \mathbf{u}\cdot\nabla\Xi' + \frac{\delta}{2}\mathrm{Pr}^{-1}\nabla^2(\Psi - \Psi'). \tag{20b}$$

We can then use definitions (10)b and (9)c and d and the reference temperature and composition profiles to rewrite Equation (20a) in the form

$$\partial_t \Psi = \mathrm{Pr}^{-1}\nabla^2\Psi + \beta u_r(\cos\alpha + \sin\alpha) - \delta\sin\alpha\nabla^2\chi, \tag{21a}$$

$$\partial_t \chi = \mathrm{Pr}^{-1}\nabla^2\chi + \beta u_r - \delta\mathrm{Pr}^{-1}\nabla^2\chi. \tag{21b}$$

Here, Equation (21b) has been obtained by subtracting Equation (20a) from Equation (20b). Equations (21a) and (21b) are only coupled together by the last term in (21a) which is multiplied by the small quantity δ and so the diffusion of χ has only a small contribution to the evolution of the buoyancy profile Ψ.

It is now reasonably easy to see the physical effects of deviating from the case of equal Prandtl numbers. For example, when $\mathrm{Sc} < \mathrm{Pr}$, so that $\delta < 0$, and with $0 < \alpha < \pi/2$ (positive compositional and thermal Rayleigh numbers) Equation (21a) shows that the growth in time of the compositional component χ has a small but destabilising effect on the buoyancy profile Ψ such that convection can now occur for lower values of Ra as $|\delta|$ becomes larger. This behaviour is well evident on the left side of Figure 5a where, upon decreasing delta from 0 to -0.5, a reduction in Ra is indeed observed. The magnitude of this reduction increases as α increases from 0 through to $\pi/2$. This is easily explained by viewing the middle panel of Figure 5b. More negative values of δ correspond to smaller values of Sc so that less energy is required for the onset of convection and both the critical Rayleigh numbers will of course decrease more. This verifies previous work (see e.g. Simitev 2011) that, for positive Rayleigh numbers, an increase in $\mathrm{R_c}$ leads to a reduction in the critical value of $\mathrm{R_t}$ required for the onset of convection.

Considering the case $\mathrm{Pr} < \mathrm{Sc}$, so that $\delta > 0$, and with $0 < \alpha < \pi/2$ $(\mathrm{R_t}, \mathrm{R_c} > 0)$, we see a similar effect occurring. Now, the diffusion of χ has a stabilising effect on the buoyancy profile, Ψ, with convection occurring at higher critical values of Ra as δ increases. This effect is in evidence on the bottom panel of Figure 6a, where an increase in Ra is seen as δ is increased. This is clearly explained by the fact that, when Sc is increased (δ increases), greater values of $\mathrm{R_c}$ are now required for the onset of convection. Again, this effect becomes larger as α increases from 0 through to $\pi/2$ as (see the middle panel of Figure 6b), after this point, it is again the composition that is controlling the onset of convection, so increasing Sc will consequently mean even greater values of $\mathrm{R_c}$are needed for the onset of convection to occur to overcome the viscous forces.

However, when $\alpha < 0$ and $|\alpha| \ll 1$, with $\mathrm{Sc} < \mathrm{Pr}$, so that $\delta < 0$, the diffusion of χ acts in an opposite way as the sign of $\sin\alpha$ changes from positive to negative. The diffusion of χ now has a stabilising effect as $\delta \sin\alpha$ is negative. This phenomenon can be seen in top panel of Figure 5b; as α changes from positive to negative we see that decreasing δ increases the thermal Rayleigh number, $\mathrm{R_t}$, whereas when $\alpha > 0$ decreasing δ decreases the critical value of $\mathrm{R_t}$. Similarly, when $\alpha > 0$ and $|\alpha| \ll 1$, with $\mathrm{Sc} > \mathrm{Pr}$, so that $\delta > 0$, the diffusion of χ leads to a reduction of the buoyancy profile. This is seen, more clearly than the previous case in the upper panel of Figure 6b. Increasing δ leads to a reduction of the critical value of $\mathrm{R_t}$. This phenomenon can be explained by the fact that, when $\alpha < 0$, the compositional buoyancy is now acting against the thermal component of buoyancy. Therefore an increase in Sc inhibits the effect of the compositional component and thus lowers the critical value of $\mathrm{R_t}$.

We have demonstrated that the departure from equal Prandtl numbers has a small but noticeable affect on the onset of convection, manifested by a deviation from the "co-density" values of Ra obtained in the case $\mathrm{Pr} = \mathrm{Sc}$. However, the regions where $\mathrm{R_t}$ and $\mathrm{R_c}$ have opposite signs, namely $-\pi/2 < \alpha < 0$ and $\pi/2 < \alpha < \pi$, will be most strongly affected as a delicate balance exists there between stabilising and destabilising forces.

An observation can be made immediately from Figures 5a and 6a, namely that the asymptotic behaviour of the null curves at $\mathrm{Pr} = \mathrm{Sc}$ when $\alpha \to -\pi/4$ and $\alpha \to 3\pi/4$ is now obeyed on only one of the sides, depending on whether Sc is larger ($\alpha \to -\pi/4$ asymptote is approached) or smaller ($\alpha \to 3\pi/4$ asymptote is approached) than Pr. In order to investigate the changes to the asymptotes, we consider next small departures from the angles $\alpha = -\pi/4$ and $3\pi/4$ by setting $\alpha = -\pi/4 + \epsilon$ and $3\pi/4 + \epsilon$, where $|\epsilon| \ll 1$, in Equation (21a) and Taylor expanding $\cos\alpha$ and $\sin\alpha$ around these values

$$\partial_t \Psi = P_t^{-1} \nabla^2 \Psi \pm \epsilon \sqrt{2} \beta u_r \pm \delta \frac{\mathrm{Pr}^{-1}}{\sqrt{2}} \nabla^2 \chi. \tag{22}$$

Here, the upper and lower signs of the $\pm$ term refers to $\alpha = -\pi/4$ and $3\pi/4$, respectively. The shift of the asymptote is a direct consequence of the coupling between Equations (21a) and (21b). We now consider the two cases $\mathrm{Pr} > \mathrm{Sc}$ ($\delta < 0$) and $\mathrm{Pr} < \mathrm{Sc}$ ($\delta > 0$) separately.

Firstly, when $\mathrm{Pr} > \mathrm{Sc}$, one can see from Equation (22) that, when $\alpha = 3\pi/4 + \epsilon$ with $\epsilon > 0$ i.e. the negative sign is taken, the diffusion of χ is destabilising and the advective term $\epsilon\sqrt{2}\beta u_r$ is stabilising. Clearly when $\delta = \epsilon = 0$ the buoyancy profile just diffuses away. As δ is decreased, the growth of the buoyancy profile is increased and thus ϵ can take greater values until the advective term becomes greater than the diffusion of χ. This is supported by the bottom panel of Figure 5a, as the asymptote of Ra is shifted further to the right when $|\delta|$ is increased. This behaviour is also observed by viewing the bottom panel of Figure 5b. One can see the shift away from the line $\alpha = 3\pi/4$ towards $\alpha = \pi$ as δ decreases from 0 to -0.5 and, as such, now lower critical values of $\mathrm{R_c}$ are required.

Secondly, when $\mathrm{Pr} < \mathrm{Sc}$ ($\delta > 0$) the asymptote shift is somewhat mirrored around $\alpha = \pi/4$ and occurs near $\alpha = -\pi/4$. When $\delta > 0$ and $\alpha = -\pi/4 + \epsilon$, the positive sign of Equation (22) shows again that the diffusion of χ and the advective term are destabilising and stabilising, respectively. Clearly, when the diffusive term can overcome the advective term, convection can occur. Therefore, as δ is increased the asymptote will shift, with negative values of ϵ of higher magnitude able to still support convection. This continues with increasing ϵ until the magnitude of the advective term becomes too large and convection is unable to occur. The bottom panel on the top of Figure 6a supports this and one may also observe the bottom panel of Figure 6b, where this time the asymptote shifts from the line $\alpha = -\pi/4$ towards $\alpha = -\pi/2$ and as such far lower critical values of $\mathrm{R_t}$ are required.

An interesting feature that occurs is the jump from small scale to large scale convection

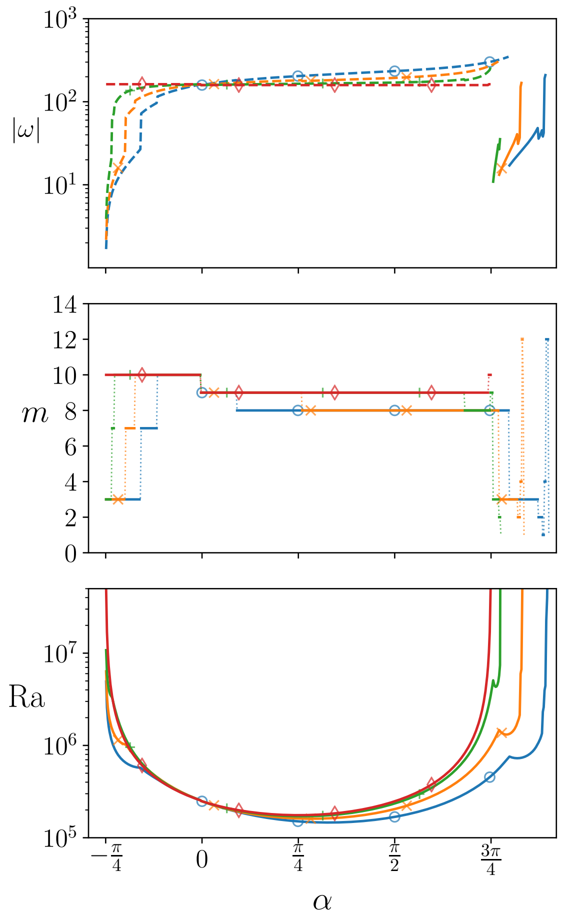

(a)

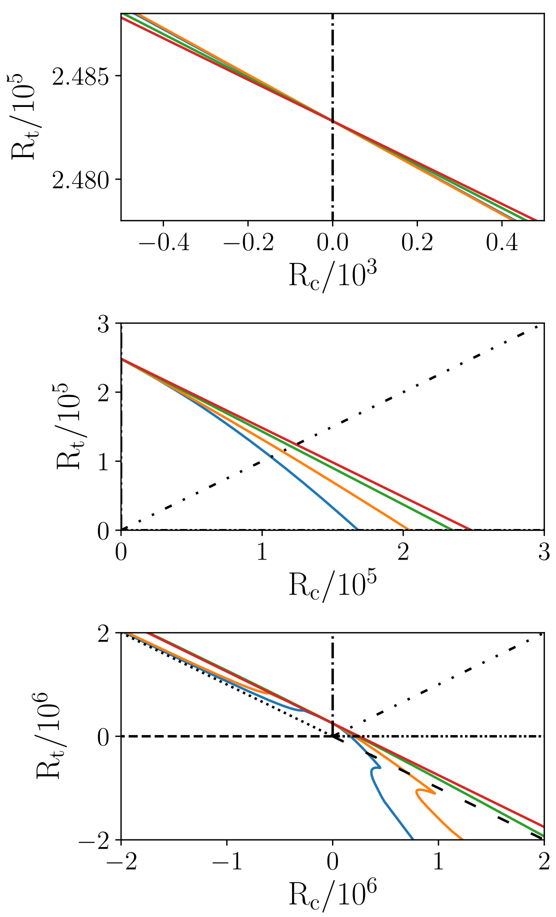

(b)

Figure 5. Linear onset of convection when the Schmidt number is taken to be just below the Prandtl number Pr = 1 with $\tau = 10^4$ for four values of δ: -0.5 (open circles), -0.3 (crosses), -0.1 (plus sign) and 0 (open circles) (a) The top panel shows the absolute values of the oscillation frequency, ω. Negative values are indicated by dashed lines whereas positive values are indicated by solid lines. The middle panel show the most unstable azimuthal wave number. The bottom panel shows the critical value of Ra. All variables shown as a function of the Rayleigh angle, α (b) The panels show three representative regions in the R_c-$R_t$plane. The dashed (▬ ▬ ▬ ▬ ▬), dotted (⋯⋯⋯), dash-dotted (▬·▬·▬·), loosely dash dot dotted (▬ · · · ▬ ·), densely dash dot dotted (▬⋯▬⋯) and loosely dashed (▬ ▬ ▬ ·) correspond to the Rayleigh angles $\alpha = -\pi/2$, $-\pi/4$, 0, $\pi/4$, $\pi/2$, $3\pi/4$, respectively.

immediately beyond the normal asymptotes ($\alpha = -\pi/4, 3\pi/4$) which occur when $\delta = 0$. The azimuthal wave-number dramatically decreases beyond the normal asymptote ($\delta = 0$) for non-zero δ (see the middle panels of Figures 5b and 6b) and a large drop in magnitude of the drift-rate ω is associated with this (see the top panels of Figures 5a and 6a). However the wave-number and drift-rate quickly rise towards the new asymptotes.

Another interesting effect occurs on the opposite side to the asymptote shifts. Here the previous asymptotes are still in effect ($\delta = 0$) but as $|\delta|$ is increased there is a reduction in the critical Rayleigh number. Again we the switch from small scale to large scale convection around these asymptotes.

Finally we mention that, the calculations shown in Figures 5 and 6 are for the specific value Pr = 1.0 but our simulations show that similar results are obtained for other values of Pr.

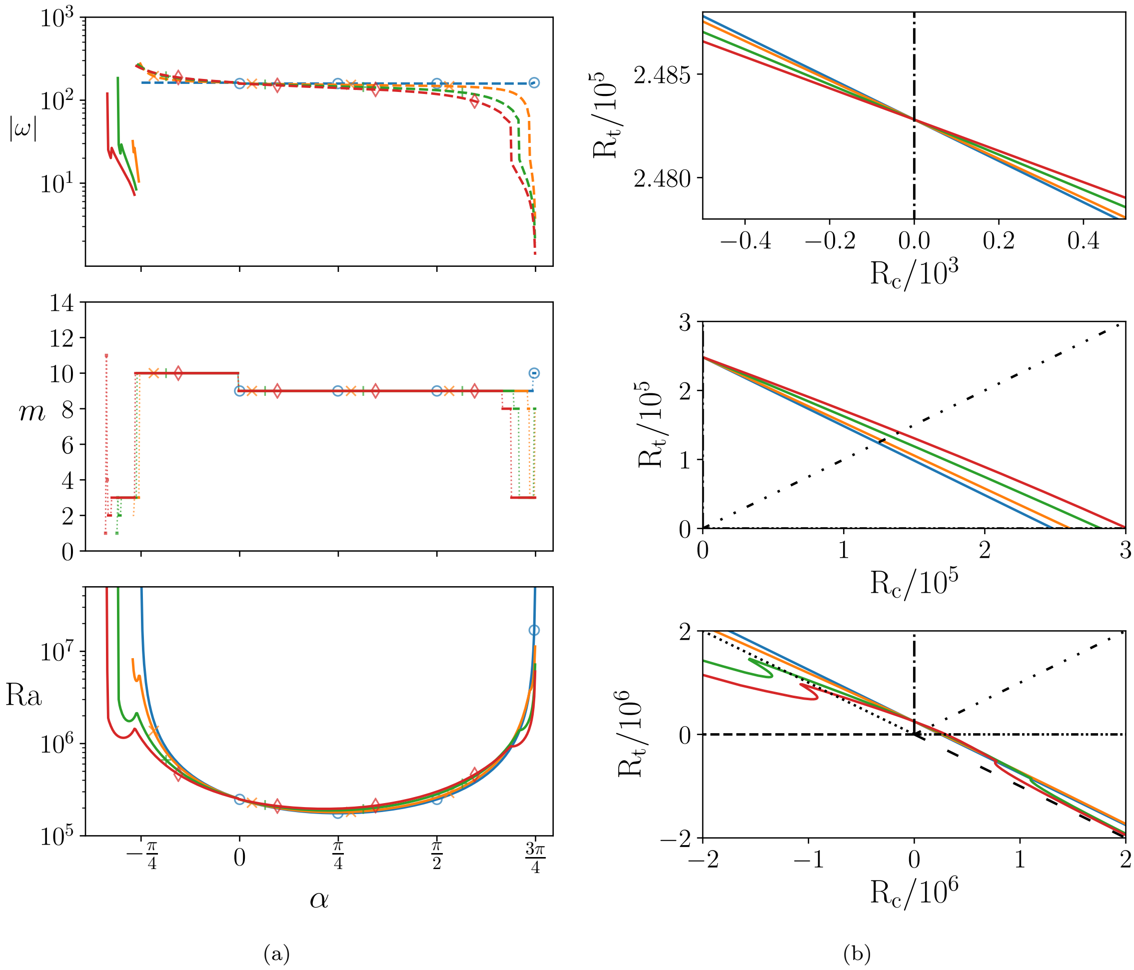

Figure 6. Same as Figure 5 but for four positive values of δ: 0 (open circles), 0.1 (crosses), 0.3 (plus sign) and 0.5 (open diamonds).

5.3. *Large differences between Prandtl numbers*

In Section 5.2 we described the asymmetries that arise in the structure of the critical Ra curves when Le differ from unity only slightly. In this section we explore what happens to these curves when Pr and Sc are significantly different so that the deviations from the Pr = Sc case become more apparent. First, recall that when Pr and Sc are significantly different Equations (13) and (14) describe the evolution of the buoyancy field Ψ well. For brevity, we will only analyse the case of Sc $\gg$ Pr as the case of Sc $\gg$ Sc is symmetric with respect to $\alpha = \pi/4$. Here Equation (14a) becomes

$$\partial_t \Psi \approx \frac{\mathrm{Pr}^{-1}}{2}\nabla^2(\Psi + \Psi') - \mathbf{u}\cdot\nabla\Xi. \tag{23}$$

The evolution of Ψ is now, essentially, only affected by the diffusion of the physical field which is characterised with the minimum value between Pr and Sc. Due to convection being radically different for values of the Prandtl numbers above and below 0.1, respectively, we present our analysis in these two cases. In the small Prandtl number limit convection is generally large scale but three distinct regions of $\mathrm{Ra}_c(\alpha)$ can be identified. In the large Prandtl number limit, four different regions, instead of three, can be identified, all which are functions of α. Figure 7 shows the results of our calculations.

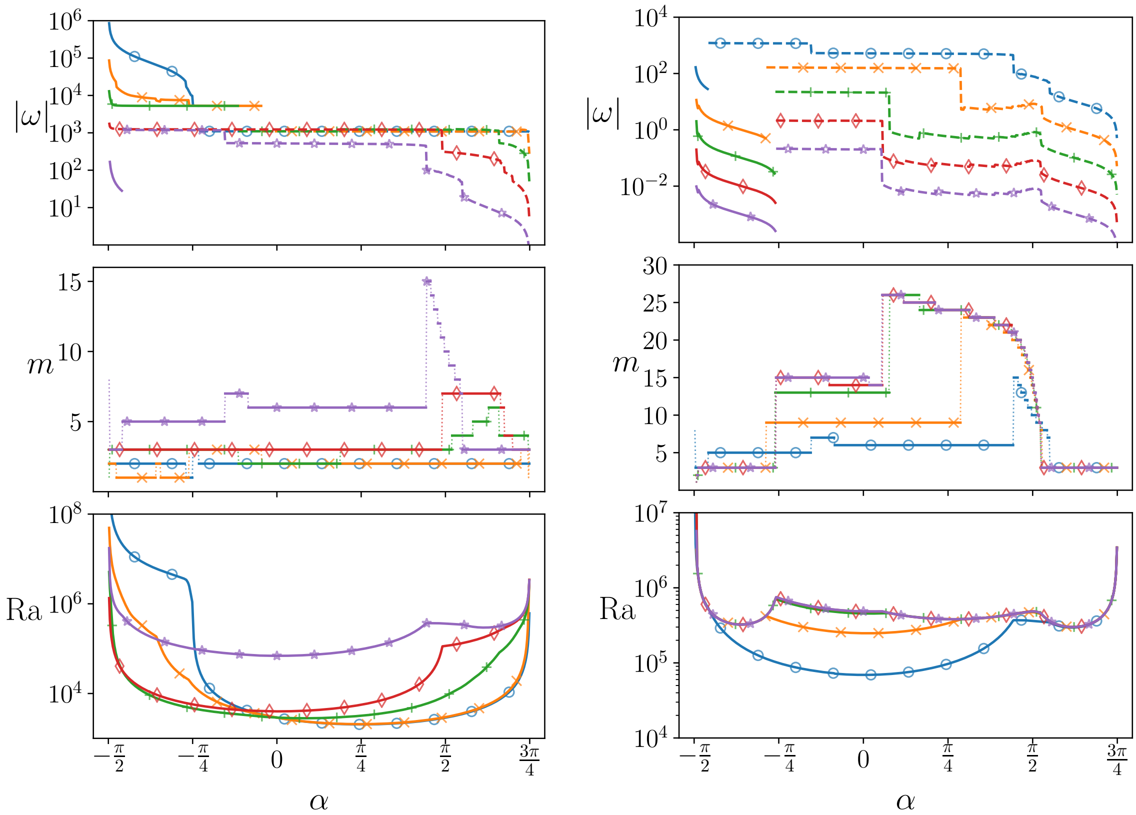

(a)

(b)

Figure 7. Linear onset of convection for value of the Schmidt number Sc = 25Pr. The rotation parameter is $\tau = 10^4$. Top, middle and bottom panels represent the drift frequency ω, the most unstable azimuthal wave number, m, and the critical effective Rayleigh number, Ra, respectively. Drift frequencies are plotted as absolute values and dashed lines correspond to the negative values (a) Low values of Pr: 10^{-5} (open circles), 10^{-4} (crosses), 10^{-3} (plus signs), 10^{-2} (open diamonds), 10^{-1} (stars) (b) High values of Pr: 10^{-1} (open circles), 1 (crosses), 10 (plus signs), 10^2 (open diamonds), 10^3 (stars).

5.3.1. *Small Prandtl number case*

For the lowest value of Pr (Figure 7a, Pr $= 10^{-5}$, light blue curves with open circles), the critical curve Ra is approximately symmetric with respect to $\alpha = \pi/4$ for values of the mixing angle between $\alpha = -\pi/4$ and $\alpha = 3\pi/4$. There, the shape of the null curves is consistent with a straight line of negative gradient in the $\mathrm{R_c} - \mathrm{R_t}$ plane. With Pr $= 10^{-5}$ we have Sc $= 2.5 \times 10^{-4}$. We see that in this regime there is very little difference between how the thermal and compositional components affect convection which is large scale ($m = 2$) with a retrograde drift ($\omega < 0$) and is of equatorially attached type. Figure 8 shows the stream function $(1/r\partial S/\partial\theta)$ in the equatorial plane for the case of Pr $= 0.0001$ (top left). This situation is easy to explain in terms of Equation (11b) as any small scale buoyancy anomalies are rapidly diffused away due to a small Prandtl number; the advection of the background profiles cannot overcome such strong diffusion.

The behaviour in the region between mixing angles $-\pi/2 > \alpha$ and $\alpha < -\pi/4$ is also easy to interpret – here the buoyancy profile Ξ has a negative sign ($\cos\alpha + \sin\alpha < 0$) and thus acts to stabilise the system. In fact, convection is only possible because the advection profile Ξ' is now approaching a maximum and therefore generates enough Ψ' to fuel the production of Ψ in Equation (11b) and consequently the velocity $\mathbf{u}$ in Equation (11a). This, however, comes at the cost of requiring a higher value of Ra for the onset of convection to take place.

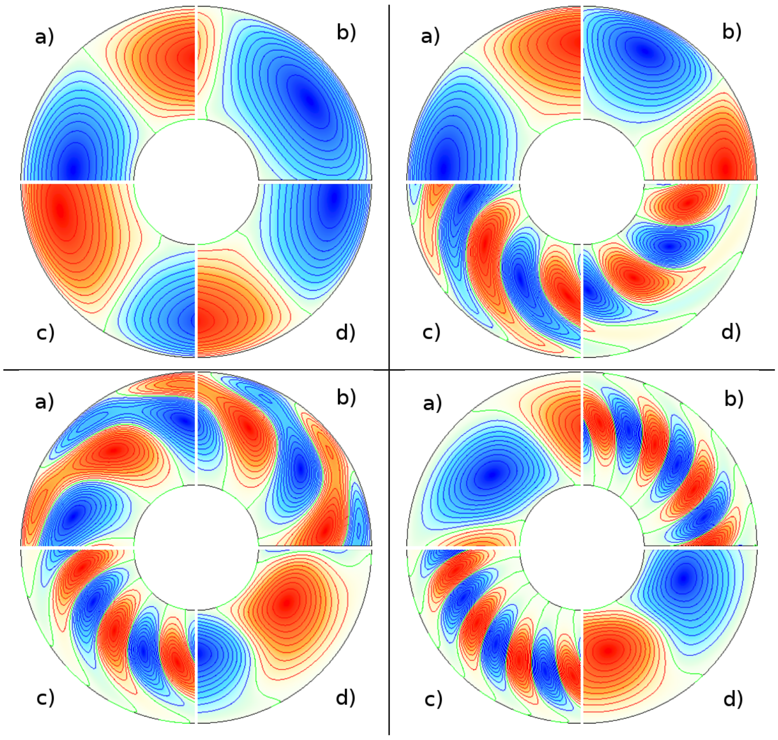

Figure 8. Stream function of the flow on the equatorial plane for four representative cases of Pr and four representative cases of α. Top left: $\mathrm{Pr} = 0.00001$; top right: $\mathrm{Pr} = 0.001$; bottom left: $\mathrm{Pr} = 0.1$; bottom right: $\mathrm{Pr} = 10$. In each panel a) corresponds to $\alpha = -3\pi/8$; b) to $\alpha = 0$; c) to to $\alpha = \pi/2$; and d) to $\alpha = 5\pi/8$.

5.3.2. *Intermediate Prandtl number case*

Increasing Pr in Figure 7a, results in a shift of the critical curve upwards and to the left. The shift in the $\mathrm{R_c} - \mathrm{R_t}$ plane is seen to the right in the direction of greater $\mathrm{R_c}$. We see a large shift to the right when $\mathrm{Pr} = 10^{-2}$, which can be explained by the fact that $\mathrm{Sc} = 2.5 \times 10^{-1}$ is greater than 10^{-1}, the value for which a change from inertial convection to viscous convection occurs. Indeed, there is a rise in wave-number from $m = 3$ to $m = 7$ so that convection is now on a smaller scale. On the top right-hand side in Figure 8c, this switch to a smaller scale convection pattern is clearly visible but it is, however, attached to both the inside and outside of the spherical shell. Increasing Pr further to a value of 10^{-1} there is a shift to the right but also a large shift in the positive $\mathrm{R_t}$ direction as again we are changing from inertially controlled convection to viscous convection. We now see an interesting effect that, as we switch from thermally controlled to compositionally controlled convection, there is a switch from large scale ($m = 6$) to a very small scale mixed convection ($m = 15$), which has already been observed by Trümper et al. (2012) but with $\mathrm{Le} = 30$. As α increases from here towards $\pi/2$ (pure compositional convection), the value of m decreases again to $m = 10$, which is equivalent to pure thermal convection with internally distributed heat sources with a Prandtl number of 2.5. Now viewing the bottom left-hand side in quadrant c of Figure 8, the convection is indeed smaller scale, with convection cells that are attached to neither in the interior nor outside of the spherical shell.

5.3.3. *Large Prandtl number case*

As mentioned before, for the case of a large thermal Prandtl number, Pr, four different regions can be identified as a function of α. Figure 7b shows the drift rate, most unstable wave number and critical effective Rayleigh number for $\mathrm{Pr} > 0.1$. In this Figure the case of $\mathrm{Pr} = 0.1$, 1, 10, 100 and 1000 is studied and at a Lewis number of $\mathrm{Le} = 25$ this corresponds to $\mathrm{Sc} = 2.5$, 25, 250, 2500 and 25000. Referring back to Equation (15) we expect that, as Pr is increased Ra and m should reach a limiting value and ω should tend to zero. This is clearly the case, as can be viewed in Figure 7b, in which all the assumptions stated above are correct as Pr increases. In Figure 8, the bottom row shows the stream function $(1/r\partial S/\partial\theta)$ on the equatorial plane for the case of $\mathrm{Pr} = 0.1$ (left) and $\mathrm{Pr} = 10$ (right). Each panel contains four representative cases of α.

For $\alpha < -\pi/4$, the gradient of the buoyancy profile Ξ changes sign with respect to $T(r)$ and $C(r)$ and is shallower. This is the same situation analysed in the previous section, where the asymptote at $\alpha = -\pi/4$ is now shifted to $\alpha = -\pi/2$ and the explanation of this phenomenon is the same. The diffusion contribution to the buoyancy field Ψ is still dominated by the temperature but it is dramatically reduced as $\cos\alpha < 1/2$. The buoyancy force, on the other hand is dominated by the composition but has changed sign, pushing regions of positive Ψ down and regions of negative Ψ up. This gives rise to large scale ($m = 3$), slow convection drifting counter-clockwise, with the value of m staying constant for $1 \leq \mathrm{Pr} \leq 10^3$ (see Figure 7b). The onset of convection occurs at lower effective Rayleigh numbers than the purely thermal case would suggest.

When α stands at around zero, $\cos\alpha \approx 1 - \alpha^2/2$ which is larger than the absolute value of $\sin\alpha$, with $\sin\alpha \approx \alpha$. Then, the temperature, which is the only quantity being diffused in Equation (14a) is also the main source of buoyancy. The system behaves like a pure thermally driven system with only one diffusivity playing a role and, as such, has the same physical structure. The onset system will present the same azimuthal wave number as the pure thermal system and drifts at the same rate with the effective Rayleigh number varying as $1/\cos\alpha$. This region is constrained between $\alpha \approx -\pi/4$ and some α larger than zero, where the diffusion of the temperature field can no longer balance the small scales generated by the advection of the full buoyancy field.

The interesting effect of mixed small-scale convection from the intermediate Prandtl number case of $\mathrm{Pr} = 10^{-1}$ can again be seen occurring in Figure 7b (open circles) in the interval $0 < \alpha < \pi/2$. However, this effect persists for higher values of Pr, with increasingly larger values of m observed. It is also noticeable that, as Pr in increased, the mixed small scales begin increasingly closer to the positive side of $\alpha = 0$, so that even a small introduction of compositional buoyancy can lead to much smaller scale convection. The effective Rayleigh number increases as Pr increases, towards a limiting value as would be expected by Equation (15) (Busse 1970).

Once we are past the pure compositional regime ($\alpha = \pi/2$), $\cos\alpha$ becomes negative; diffusion then acts to concentrate anomalies of Ψ around the anomalies of Θ instead of dispersing them. However, because Ξ is now smaller than either of T or C, there will be less buoyancy produced by advection. This leads to a situation where large scales are preferred with a sharp drop in m occurring in Figure 7b towards a constant value of $m = 3$. The critical effective Rayleigh number is also reduced and translates to a reduction $\mathrm{R_c}$ in the $\mathrm{R_c}$-$\mathrm{R_t}$ plane.

The right asymptote for α is still at $3\pi/4$ as was the case in Figure 6 with $\mathrm{Sc} > \mathrm{Pr}$, although the small reduction in Ra that exists there, near the asymptote, is now much larger and extends close to $\alpha = \pi/2$, depending on the value of Pr.

6. Dependence on the Coriolis number

So far we have analysed cases at fixed Coriolis number, τ. It is well known, however, that the critical Rayleigh number will depend on this adimensional parameter. In the case of purely thermal convection, the thermal Rayleigh number $\mathrm{R_t}$ is proportional to $\tau^{4/3}$ (see Equation (15)). Here, we will show that the effective Rayleigh number for double buoyant, double diffusive convection obeys the same scaling law in regions where the lowest diffusion quantity dominates in generating buoyancy or when both Rayleigh numbers are positive.

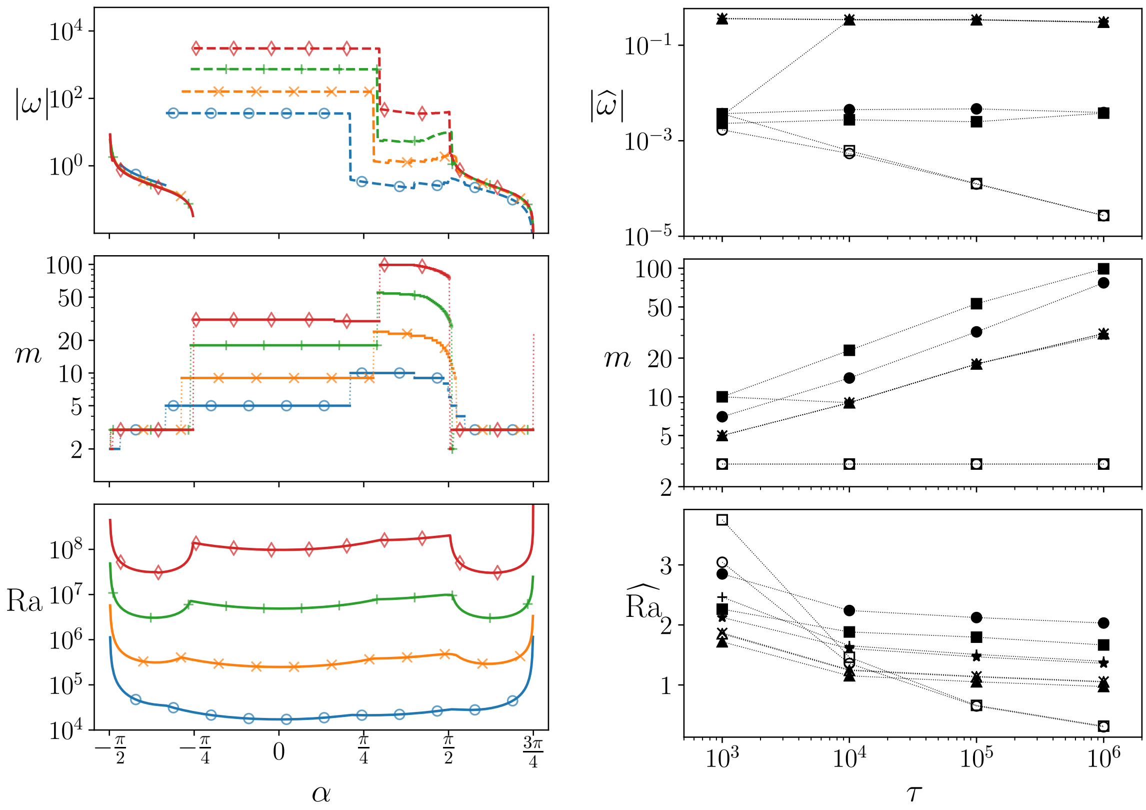

(a) (b)

Figure 9. (a) Linear onset of convection with Coriolis number, τ, taking the values 10^3 (open circles), 10^4 (crosses), 10^5 (plus sign) and 10^6 (open diamonds). The top panel contains the drift frequency of the system in absolute value. Solid lines represent positive values and dashed lines, negative values. The middle panel contains the most unstable azimuthal wave number. Note that the vertical scale is logarithmic. The bottom panel shows the effective Rayleigh number at onset. Note that $\alpha = -\pi/2$ and $\alpha = 3\pi/4$ are asymptotes for Ra and all curves should extend to infinity as α tends to those points. (b) Linear onset of convection as a function of the Coriolis number τ for different values of $\alpha_i = -3\pi/8$ (open squares), $-\pi/4$ (plus sign), $-\pi/8$ (crosses), 0 (filled triangle), $\pi/8$ (open triangle), $\pi/4$ (stars), $3\pi/8$ (filled square), $\pi/2$ (filled circle), $5\pi/8$ (open circle) ($i = 1-9$). In particular, open squares have negative compositional Rayleigh number and open circles have negative thermal Rayleigh number. Filled squares correspond to the mixed small scale, compositionally dominated convective regime and stars to the medium scale, thermally dominated regime. The top panel shows the scaled drift-rate, $\widehat{\omega} = \omega\tau^{-2/3}$, the middle panel the most unstable azimuthal wave number; the bottom panel shows the critical values of the scaled effective Rayleigh number $\widehat{\mathrm{Ra}} = \mathrm{Ra}\tau^{-4/3}$.

In Figure 9a we present results where both Prandtl numbers are above unity (Pr = 1, Sc = 100). In this case, both pure one-buoyant onset patterns of flow are consistent with rotating convection featuring z-aligned columns centred at mid shell in the equatorial plane. This is consistent with the results in Section 5.3. The "boat-shaped" plots are similar to those in Figure 9a as we are in the Sc $\gg$ Pr regime i.e large Lewis number regime.

We observe a region symmetric around $\alpha = 0$ where buoyancy is generated by the thermal component of buoyancy as it has the lowest Prandtl number. The most unstable azimuthal wave number is constant across this region. The region where buoyancy is dominantly generated by the compositional component occurs approximately between $\alpha = \pi/4$ and $\alpha = \pi/2$. This region is characterised by a sudden jump to very small scale convection near $\alpha = \pi/4$ and a gradual shift to larger scales that are associated with one-buoyancy compostional convection at $\alpha = \pi/2$.

Two regions of very large scale convection appear in the octants $[-\pi/2, -\pi/4]$ and $[\pi/2, 3\pi/4]$. These regions are characterised by opposite signed Rayleigh numbers. This shape and convective structure were already explained in Section 5.3.

Figure 9b shows the evolution and possible scaling of $\widehat{\mathrm{Ra}} = \mathrm{Ra}\tau^{-4/3}$, m and $\widehat{\omega} = \omega\tau^{-2/3}$ as a function of τ for these regions. It was constructed from Figure 9a by extracting points at $\alpha_i = -3\pi/8$, $-\pi/4$, $-\pi/8$, 0, $\pi/8$, $\pi/4$, $3\pi/8$, $\pi/2$, $5\pi/8$, with i varying between 1 and 9. Intermediate points in τ to those in Figure 9b were directly computed for the given values of α.

Most of the domain obeys a thermal type scaling $\mathrm{Ra} \propto \tau^{4/3}$ and number m also follows a thermal type scaling $m \propto \tau^{1/3}$ that we expect in the small Ekman number limit i.e. Equation (15) (Busse 1970). The purely thermal case occurs when $\alpha = 0$ (filled triangles) so that $\mathrm{Ra} = \mathrm{R_t}$. Then for this particular value, Figure 9b corresponds to the curve for $P = 1.0$ in Figure 3 in the investigation by Ardes et al. (1997), although there will be a slight discrepancy as $\eta = 0.4$ in that case. As α diverges from zero in both the positive and negative directions, it is clear from Figure 9b that Ra increases which is just due to the fact that convection is thermally dominated due to the large Lewis number and in reality the thermal Rayleigh number stays reasonably constant. However, when $\alpha = \pi/2$ (filled circles) the convection is purely compositional so that $\mathrm{Ra} = \mathrm{R_c}$ which is essentially the same as thermal convection but with Prandtl number 100. Again, we note the jump to small-scale mixed convection when $\alpha = 3\pi/8$.

A different scaling occurs on the two large scale regions sampled by points $i = 1$ and $i = 9$. These are the regions previously described as arising from large discrepancies in Prandtl numbers. The most unstable azimuthal wave number in these regions seems to be independent of the Coriolis number, τ, and the critical effective Rayleigh number is now $\mathrm{Ra} \propto \tau$.

Note that, because these new regions obey a shallower scaling of Ra with τ, as this parameter grows, those large scale regions will have a lower critical value of Ra when compared to pure thermal or compositional convection.

Significant deviations from the proposed scaling seem only to occur for small values of the Coriolis number. This is to be expected as then, inertial rather than rotating convection is preferred.

7. Dependence on the shell thickness

Finally, we explore what happens when we change the radius ratio. This type of analysis is important because of its applicability to planetary contexts, but also because, on the course of their lifetimes, planetary cores undergo a reduction of the convective shell; systems that were convecting at a certain shell thickness may stop convecting and vice versa. Figure 10a shows how both the Rayleigh number, the most unstable wave number and the drift-rate vary with η.

As in the previous section, we used $\mathrm{Pr} = 1.0$, $\mathrm{Sc} = 100.0$ but now fixed $\tau = 10^4$. As expected if the structure of convection changes only due to the changes in geometry, the effective Rayleigh number decreases as η tends to 1. The most unstable wave number, however, increases with η as would be expected when the equatorial perimeter tends to infinity. However, the exact dependences observed are not strictly as could be expected from a pure geometrical reasoning.

Figure 10b shows, for selected values of α, the values and scaling, based off Equation (15), of $\bar{\omega} = \omega(1-\eta)^{-2/3}$, m and $\bar{\mathrm{Ra}} = \mathrm{Ra}(1-\eta)^{-10/3}$ as a function of η. There, it is easier to see that the functional dependency of $\mathrm{Ra}(\eta)$ also depends on the type of buoyancy that dominates. Filled triangles correspond to pure thermal convection and filled circles to pure compositional convection. Open squares have negative compositional Rayleigh number and open circles have negative thermal Rayleigh number. Filled squares correspond to the mixed small scale, compositional dominated convective regime and stars to the medium scale, thermally dominated regime.

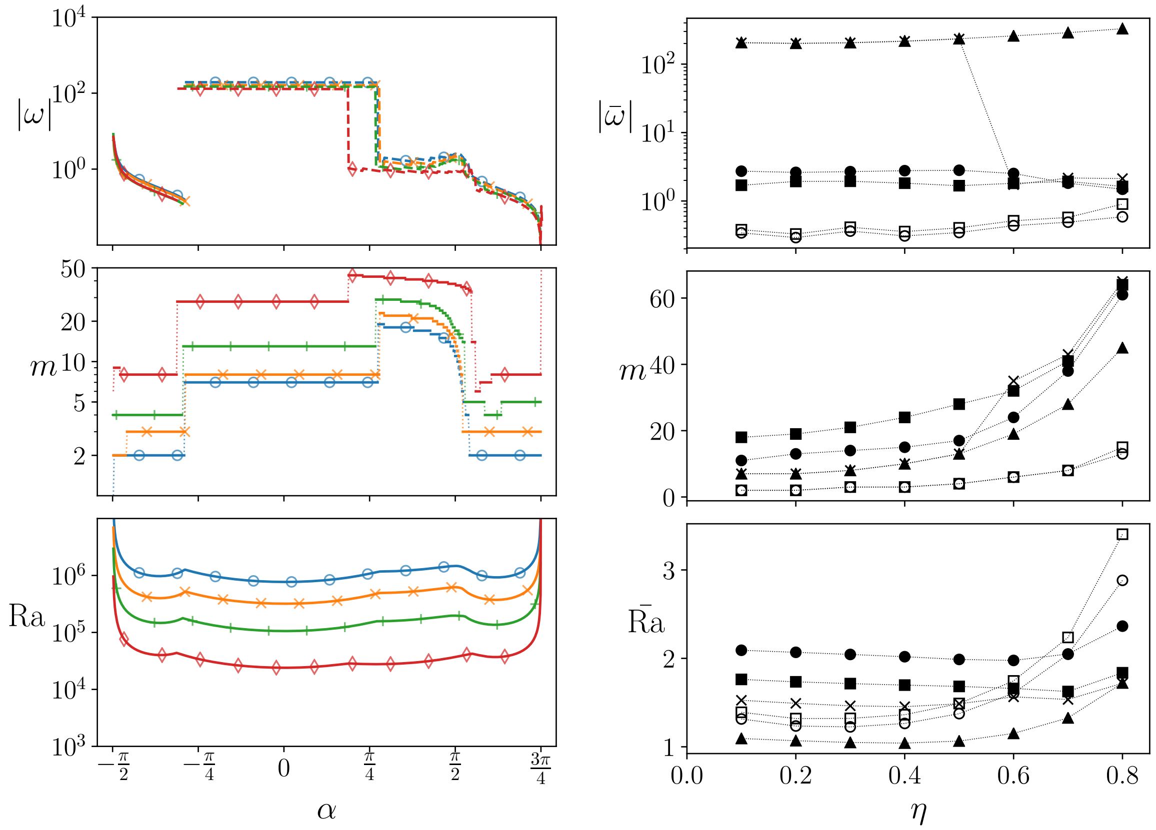

(a) (b)

Figure 10. (a) Linear onset of convection for shell thickness, η, varying from 0.1 (unfilled circles), 0.3 (crosses), 0.5 (plus sign) and 0.7 (unfilled diamond). As in previous "boat plots", the top panel, shows the drift rate, the middle plot shows the most unstable azimuthal wave numbers and the bottom panel shows the critical effective Rayleigh number (b) Linear onset of convection as a function of the radius ratio for selected values of $\alpha = -3\pi/8$ (open squares), 0 (filled triangles), $\pi/4$ (crosses), $3\pi/8$ (filled squares), $\pi/2$ (filled squares), $3\pi/4$ (open circles). Filled triangles correspond to pure thermal convection and filled circles to pure compositional convection. Open squares have negative compositional Rayleigh number and open circles have negative thermal Rayleigh number. Filled squares correspond to the mixed small scale, compositional dominated convective regime and stars to the medium scale, thermally dominated regime. The top panel shows the scaled drift-rate, $\bar{\omega} = \omega(1-\eta)^{-2/3}$, the middle panel the most unstable azimuthal wave number and the bottom panel the scaled effective Rayleigh number, $\bar{\text{Ra}} = \text{Ra}(1-\eta)^{-10/3}10^{-6}$.

The scaling used is fairly reasonable for low to intermediate values of $\eta \in [0.1, 0.5]$ when $\alpha =$ 0, $\pi/4$, $3\pi/8$ and $\pi/2$. However, after this value, there is a change from constant dependence and the solutions begin to diverge, as the approximation given by Equation (15) (Busse 1970) begins to break down.

When the system is stabilised by one quantity but destabilised by the other (points $i = 1$ and $i = 9$) then the most unstable wave number is proportional to the mean radius and the effective Rayleigh number, to the square of the radius at 44% of the shell.

8. Discussion and conclusions

In this paper we identified the possible deviations of the onset of doubly buoyant, doubly diffusive rotating convection from a pure thermal regime. We constructed a new representation for the thermal and compositional Rayleigh numbers that makes it possible to define a strictly positive pre-factor for the buoyancy. This pre-factor is the effective Rayleigh number, Ra which, in this new representation, has a unique critical value for all other parameters fixed.

This is in contrast to what happens when $\mathrm{R_t}$ and $\mathrm{R_c}$ are used with one of them fixed. The trade-off between thermal and compositional buoyancy is now determined by a mixing angle α which takes positive values in the right half of the $\mathrm{R_t} - \mathrm{R_c}$ plane.

In the case of equal values of the Prandtl number and the Schmidt number, the system behaves as a single-diffusive, one-buoyancy system. The critical curve is a straight line with slope -1 in the $\mathrm{R_t} - \mathrm{R_c}$ plane and behaves like $1/(\cos\alpha + \sin\alpha)$ in $\mathrm{Ra} - \alpha$ space. In this case asymptotes for the critical curve stand at $-\pi/4$ and $3\pi/4$.

Still in $\mathrm{Ra} - \alpha$ space, as the Prandtl numbers deviate from each other, small deviations appear that shift the asymptotes on one of the sides and reduce Ra on both sides. The largest changes appear on the octants adjacent to the asymptotes of the equal diffusility case. The structure of the $\mathrm{Ra}_c(\alpha)$ curve is qualitatively preserved with variations of τ or η.

When the values of the Prandtl and the Schmidt numbers are significantly differ from each other three possible cases can take place. In all cases, asymptotes stand at $\alpha = -\pi/2$ and $\alpha = 3\pi/4$ when $\mathrm{Sc} \gg \mathrm{Pr}$ and at $\alpha = -\pi/4$ and $\alpha = \pi$ when $\mathrm{Pr} \gg \mathrm{Sc}$. When both Prandtl numbers are below 0.1 very large scale inertial convection dominates independently of α. When both Prandtl numbers are above 0.1, rotating convection takes place with a variety of wave numbers depending on α. Mixed, very small-scale, convection can occur when $\mathrm{Pr} > 0.1$, where we have seen in Figure 7 that as Pr increases the mixed small scales become increasingly smaller whereas for low Prandtl number, inertial convection, there is no mixed small scale convection at positive values of $\mathrm{R_c}$ and $\mathrm{R_t}$. This is a result already found in (Trümper et al. 2012) but there only a single case $\mathrm{Pr} = 0.1$ was studied as opposed to our a full Prandtl number investigation.

Most of this study was carried out for large values of τ and relatively large values of Prandtl and Schmidt numbers. We therefore were, to a certain extent, reasonably well able to compare our work to the asymptotic study Busse (1970), Zhang (1994), Busse (2002). In the limit $\mathrm{Pr} \to \infty$ it was found from Figure 7b that Ra and m increased towards a limiting values and the drift-rate decreased in magnitude towards zero, mirroring the pure thermal case. In our study of the critical values dependence on τ, it was found that, for $\mathrm{Pr} = 1.0$ and $\mathrm{Le} = 100$, the dependence followed a thermal type rotating convection scaling as in Busse (1970), given by Equation (15), as long as the regime of large scale convection with either $\mathrm{R_t} < 0$, $\mathrm{R_c} > 0$ or $\mathrm{R_t} < 0$, $\mathrm{R_c} > 0$ was not considered. In those regions, $\mathrm{Ra} \propto \tau$, while the preferred azimuthal wave number m showed no variation with respect to τ and the drift rates $|\omega| \propto \tau^{2/3}$. A thermal type scaling was also seen when varying η but only for relatively thick shells $\eta \in (0.1, 0.5)$ beyond which the approximation given by Equation (15) starts to break down. Again this thermal scaling is only correct as long as the regime of large scale convection with either $\mathrm{R_t} < 0$, $\mathrm{R_c} > 0$ or $\mathrm{R_t} < 0$, $\mathrm{R_c} > 0$ was not considered.

In regions of parameter space where $\mathrm{R_t}$ or $\mathrm{R_c}$ are negative, only very large scale convection seems to be possible. This happens when $\alpha < 0$ or $\alpha > \pi/2$. Convection is not possible when the quantity with the lowest Prandtl number and a negative Rayleigh number dominates buoyancy. When the quantity with the lowest Prandtl number and a negative Rayleigh number does not dominate the buoyancy budget, convection is very large scale and has a negative drift rate.

Acknowledgements

This work was supported by the Leverhulme Trust [grant number RPG-2012-600].

References

M. Ardes, F. H. Busse, and J. Wicht. Thermal convection in rotating spherical shells. *Phys. Earth Plan. Int.*, 99:55 – 67, 1997. doi:10.1016/S0031-9201(96)03200-1.

S. Braginsky and P. H. Roberts. Equations governing convection in earth's core and the geodynamo. *Geophys. Astrophys. Fluid Dyn.*, 79:8, 1995. doi:10.1080/03091929508228992.

S. I. Braginsky. Structure of the F layer and reasons for convection in the Earth's core. *Soviet Phys. Dokl.*, 149:8–10, 1963.

M. Breuer, A. Manglik, J. Wicht, T. Trümper, H. Harder, and U. Hansen. Thermochemically driven convection in a rotating spherical shell. *GJI*, 183:150–162, 2010. doi:10.1111/j.1365-246X.2010.04722.x.

F. Busse and R. Simitev. Parameter dependences of convection-driven dynamos in rotating spherical fluid shells. *Geophys. Astrophys. Fluid Dyn.*, 100:341, 2006. doi:10.1080/03091920600784873.

F. Busse and R. Simitev. Planetary dynamos. In *Treatise on Geophysics*, pages 239–254. Elsevier, 2015. doi:10.1016/b978-0-444-53802-4.00172-x.

F. H. Busse. Thermal instabilities in rapidly rotating systems. *Journal of Fluid Mechanics*, 44(03):441, nov 1970. doi:10.1017/s0022112070001921.

F. H. Busse. Is low Rayleigh number convection possible in the Earth's core? *Geophysical Research Letters*, 29 (7), 2002. doi:10.1029/2001gl014597.

F. H. Busse and R. Simitev. Inertial convection in rotating fluid spheres. *Journal of Fluid Mechanics*, 498: 23–30, 2004. doi:10.1017/S0022112003006943.

U. Christensen and J. Wicht. Numerical dynamo simulations. In *Treatise on Geophysics*, pages 245–277. Elsevier, 2015. doi:10.1016/b978-0-444-53802-4.00145-7.

U. R. Christensen. Iron snow dynamo models for Ganymede. *Icarus*, 247:248–259, feb 2015. doi:10.1016/j.icarus.2014.10.024.

C. Davies, M. Pozzo, D. Gubbins, and D. Alfè. Constraints from material properties on the dynamics and evolution of Earth's core. *Nature Geoscience*, 8, 2015. doi:10.1038/NGEO2492.

G. Glatzmaier. *Introduction to Modeling Convection in Planets and Stars: Magnetic Field, Density Stratification, Rotation*. Princeton Series in Astrophysics. Princeton University Press, 2013. ISBN 9781400848904.

K. Hori, J. Wicht, and U. Christensen. The influence of thermo-compositional boundary conditions on convection and dynamos in a rotating spherical shell. *Physics of the Earth and Planetary Interiors*, 196-197: 32–48, apr 2012. doi:10.1016/j.pepi.2012.02.002.

J. A. Jacobs. The Earth's Inner Core. *Nature*, 172:297–298, Aug. 1953. doi:10.1038/172297a0.

R. Jeanloz. The nature of the earth's core. *Annual Review of Earth and Planetary Sciences*, 18:357–386, 1990. doi:10.1146/annurev.ea.18.050190.002041.

C. A. Jones. Planetary magnetic fields and fluid dynamos. *Annual Review of Fluid Mechanics*, 43(1):583–614, 2011. doi:10.1146/annurev-fluid-122109-160727.

R. Kippenhahn, A. Weigert, and A. Weiss. *Stellar Structure and Evolution*. Springer Berlin Heidelberg, 2012. doi:10.1007/978-3-642-30304-3.

J. R. Lister and B. A. Buffett. The strength and efficiency of thermal and compositional convection in the geodynamo. *Physics of the Earth and Planetary Interiors*, 91(1):17 – 30, 1995. ISSN 0031-9201. doi:10.1016/0031-9201(95)03042-U. Study of the Earth's Deep Interior.

A. Manglik, J. Wicht, and U. R. Christensen. A dynamo model with double diffusive convection for Mercury's core. *Earth and Planetary Science Letters*, 289(3-4):619–628, jan 2010. doi:10.1016/j.epsl.2009.12.007.

M. Net, F. Garcia, and J. Sánchez. Numerical study of the onset of thermosolutal convection in rotating spherical shells. *Physics of Fluids*, 24(6):064101, jun 2012. doi:10.1063/1.4723865.

P. Olson, M. Landeau, and E. Reynolds. Dynamo tests for stratification below the core-mantle boundary. *Physics of the Earth and Planetary Interiors*, 271:1–18, oct 2017. doi:10.1016/j.pepi.2017.07.003.

E. Plaut and F. H. Busse. Multicellular convection in rotating annuli. *Journal of Fluid Mechanics*, 528:119–133, apr 2005. doi:10.1017/s0022112004003180.

M. Pozzo, C. Davies, D. Gubbins, and D. Alfè. Thermal and electrical conductivity of iron at Earth's core conditions. *Nature*, 485:355 – 358, 2012. doi:10.1038/nature11031.

K. Röttger, A. Endriss, J. Ihringer, S. Doyle, and W. F. Kuhs. Lattice constants and thermal expansion of H_2O and D_2O ice I*h* between 10 and 265 K. *Acta Crystallographica Section B*, 50(6):644–648, Dec 1994. doi:10.1107/S0108768194004933.

L. A. C. Silva and R. D. Simitev. Spectral code for linear analysis of the onset of thermo-compositional convection in rotating spherical fluid shells. *Zenodo*, 2018. doi:10.5281/zenodo.1307245.

R. Simitev and F. Busse. Patterns of convection in rotating spherical shells. *New J. Phys.*, 5:97, 2003. doi:10.1088/1367-2630/5/1/397.

R. D. Simitev. Double-diffusive convection in a rotating cylindrical annulus with conical caps. *Phys. Earth Plan. Int.*, 186:183–190, 2011. doi:10.1016/j.pepi.2011.04.007.

S. W. Squyres, R. T. Reynolds, P. M. Cassen, and S. J. Peale. The Evolution of Enceladus. *Icarus*, 53(2):319 – 331, 1983. doi:10.1016/0019-1035(83)90152-5.

F. Takahashi. Double diffusive convection in the Earth's core and the morphology of the geomagnetic field . *Phys. Earth Planet. Int.*, 226(0):83–87, 2014. ISSN 0031-9201. doi:10.1016/j.pepi.2013.11.006.

S. Takehiro and Y. Sasaki. Penetration of steady fluid motions into an outer stable layer excited by MHD thermal convection in rotating spherical shells. *Physics of the Earth and Planetary Interiors*, 276:258–264, mar 2018. doi:10.1016/j.pepi.2017.03.001.

T. Trümper, M. Breuer, and U. Hansen. Numerical study on double-diffusive convection in the Earth's core. *Phys. Earth and Planet. Inter.*, 194-195:55–63, 2012. doi:10.1016/j.pepi.2012.01.004.

K. Zhang. On coupling between the poincaré equation and the heat equation. *Journal of Fluid Mechanics*, 268:211–229, 1994. doi:10.1017/S0022112094001321.

K. Zhang and X. Liao. *Theory and Modeling of Rotating Fluids.* Cambridge University Press, 2017. doi:10.1017/9781139024853.

K.-K. Zhang and F. H. Busse. On the onset of convection in rotating spherical shells. *Geophys. Astrophys. Fluid Dynamics*, 39:119 –147, 1987. doi:10.1080/03091928708208809.